

The importance of thermal dissociation in CO₂ microwave discharges investigated by power pulsing and rotational Raman scattering

D. C. M. van den Bekerom, J. M. Palomares Linares, T. Verreycken, E. M. van Veldhuizen, S. Nijdam, G. Berden, W. A. Bongers, M. C. M. van de Sanden, G. J. van Rooij

DIFFER, De Zaale 20, 5612AJ Eindhoven, The Netherlands

E-mail: g.j.vanrooij@diffier.nl

25 October 2018

D. C. M. van den Bekerom et al. 2019 Plasma Sources Sci. Technol. 28 055015

DOI: 10.1088/1361-6595/aaf519

Abstract. The input power of a CO₂ microwave plasma is modulated at kHz rate in scans of duty cycle at constant average power to investigate gas heating dynamics and its relation to dissociation efficiency. Rotational temperature profiles obtained from rotational Raman scattering reveal peak temperatures of up to 3000 K, while the edge temperature remains cold (500 K). During the plasma “OFF”-period, the gas cools down convectively, but remains overall too hot to allow for strong overpopulation of vibrational modes (2200 K in the core). Fast optical imaging monitors plasma volume variations and shows that power density scales with peak power. As dissociation scales with observed peak rotational temperature, it is concluded that thermal processes dominate. A simple 0D model is constructed which explains how higher power density favors dissociation over radial energy transport. Thermal decomposition is reviewed in relation to quenching oxygen radicals with vibrationally excited CO₂, to reflect on earlier reported record efficiencies of 90 %.

1. Introduction

1.1. Background and outline

Microwave plasmas are widely investigated in view of their potential to provide highly efficient CO₂ conversion [Rusanov et al., 1981, Ageeva et al., 1986, Fridman, 2008, Legasov et al., 1978, Asisov et al., 1981, Asisov et al., 1983, Goede et al., 2013, Silva et al., 2014, van Rooij et al., 2015, Chen et al., 2017, Snoeckx et al., 2015, den Harder et al., 2016, Bongers et al., 2016, Britun et al., 2018]. Energy efficiencies up to 90 % have been reported in the 80s for a flowing microwave plasma reactor similar to the one under investigation in this paper. These high efficiencies have traditionally been explained by

predominant vibrational excitation driving a strong non-equilibrium between vibrational and translational degrees of freedom, which in turn intensifies dissociation.

Recent attempts to reproduce the high efficiencies previously observed have so far been unsuccessful [Silva et al., 2014, Snoeckx et al., 2015, den Harder et al., 2016, Britun et al., 2018]. In recent work reported from our own lab by Den Harder [den Harder et al., 2016], efficiencies close to 50% have been reached. Temperature measurements revealed that high efficiencies are correlated to high temperatures. The correlation between core temperature and efficiency suggests that thermal chemistry plays an important part in the investigated CO₂ plasmolysis. Rayleigh scattering measurements indicated temperatures in the plasma core exceeding 3500 K. A two-temperature model was suggested to explain the mismatch between measured conversion and the conversion that was expected at the measured temperatures. In the two-temperature model, the plasma consists of two well-separated zones: a hot core and a cold shell.

These experiments are extended in the current paper by pulsing the microwave power. Power pulsing allows decoupling of mean and peak power by varying the duty cycle of the power pulse. Decoupling peak and mean power provides insights into dissociation mechanisms, since the peak power is related to electron production while the average power is related to thermodynamic parameters of the plasma like the average gas temperature. Additionally, by modulating the power the gas can cool down during the plasma “OFF”-time, potentially preventing the vibrational quenching threshold temperature to be reached.

Temperatures reported by Den Harder were measured by Rayleigh scattering [den Harder et al., 2016]. Because the Rayleigh scattering cross-section depends on the composition of the mixture, assumptions on the composition were necessary to determine an effective cross-section [den Harder et al., 2016, van den Bekerom et al., 2017]. In the current paper, temperatures are measured without the need for assumptions on composition by employing rotational Raman scattering on CO₂, which was recently developed for use at high temperatures [van den Bekerom et al., 2018]. Temperatures can be obtained from rotational Raman spectra with higher confidence compared to Rayleigh scattering because the temperature is obtained by fitting a spectrum instead of measuring the intensity of a signal. Like Rayleigh scattering, the Raman scattering measurements are spatially and temporally resolved yielding spatial temperature profiles of the plasma.

The kinetic model presented by Den Harder is further developed. The previous model was only valid for a fixed volume in the afterglow where no heat sources are present and was used exclusively for modeling quenching dynamics. In this paper the 0-D model is upgraded to include flowing volumes that are heated by an external power source (i.e. the plasma). The two-temperature model will be incorporated by simulating two separate volumes that can exchange heat with each other.

1.2. The potential of microwave pulsing

Microwave pulsing has been used frequently for studying plasma dynamics [Lieberman and Ashida, 1996, Baeva et al., 2001, Hbner et al., 2014, Kabouzi and Moisan, 2005, Repsilber et al., 2004, Carbone and Nijdam, 2014, Carbone and Nijdam, 2015]. In this section, we will review applications of plasma pulsing reported in literature. In oxygen plasmas, power interruption showed fast electron detachment of O⁻ and O₂⁻ after the discharge, rapidly increasing the electron density [Baeva et al., 2001]. A rotational-vibrational non-equilibrium was observed until it thermalized after 1 ms. In a pulsed microwave discharge in nitrogen, production of ground state atomic nitrogen was found after switching off the plasma. [Repsilber et al., 2004]. This was attributed to electronically excited atomic nitrogen decaying to the electronic ground state after the pulse.

Noble gas plasmas are ideally suited for generic plasma discharge studies because of their simple chemistry. Neon discharges were used for studying plasma filamentation [Kabouzi and Moisan, 2005], while argon discharges were used for characterization of plasma ignition effects by employing Thomson scattering and ICCD imaging at different pressures and pulse repetition rates [Carbone and Nijdam, 2015, Carbone and Nijdam, 2014]. The plasma OFF-time, the duration of time when the plasma is off, was found to be the determining parameter in the ionization dynamics. Compared to steady state operation, the population of Ar 4s states were significantly higher in pulsed plasmas with a repetition rate of a few kHz. The post-discharge electron temperature was investigated in the same setup for different admixtures of H₂, O₂, N₂ and CO₂ [Hbner et al., 2014]. It was found that for both N₂ and CO₂ the electron temperature remained comparatively high (0.8 eV) because of superelastic collisions between electrons and vibrationally excited molecules.

In addition to studying plasma dynamics, pulsed plasmas can enhance chemical reactivity through independent tuning of the mean and peak power densities. Because of its application in film deposition, a lot of work has been done on microwave discharges in H₂ and CH₄ [Rousseau et al., 2004, Stancu et al., 2005, Rousseau et al., 1994, Koldanov et al., 2005, Duten et al., 2002]. By adjusting the mean power density in hydrogen plasmas, microwave pulsing allows independent control over relative atomic hydrogen content [Rousseau et al., 1994, Rousseau et al., 2004, Stancu et al., 2005]. This is explained by considering the role of quartz in the recombination of atomic hydrogen: a higher wall temperature leads to higher atomic surface recombination and therefore reduces the relative atomic hydrogen fraction. The mean volumetric power density can be lowered by decreasing the duty cycle which reduces the wall temperature, thereby reducing losses due to recombination/back-reactions – a strategy that may work in CO₂ plasmas as well. In effect, the hydrogen plasma can be optimized for neutral production, increasing atomic hydrogen molar fractions from 30 to 100 % at the same mean power [Rousseau et al., 1994]. Moreover, analyzing the time-resolved kinetics revealed that the vibrational excitation of hydrogen as well as chemical reactions play an important role in establishing the energy balance of the discharge

[Koldanov et al., 2005]. In the CW-discharge, the rotational temperature was found to be in equilibrium with the gas temperature, while in a pulsed discharge the system equilibrated only 100 μ s after the beginning of the pulse [Duten et al., 2002]. During the pulse, the gas temperature climbs to a maximum and then decreases until it reaches a steady state value that was below the CW-discharge temperature. This temperature maximum was shown to be limited by molecular dissociation [Koldanov et al., 2005]. The improved control over atomic hydrogen production by pulsing power translates e.g. to more control over growth rate in diamond deposition [Hassouni et al., 2001], with low temperature growth rates in pulsed discharges increased by a factor of 20 to 50 compared to CW-discharges [Ring et al., 1995].

Another application of microwave plasmas is the vibrational pumping of CO₂ lasers, which involves aspects similar to those relevant for non-equilibrium CO₂ dissociation. It was shown that the use of pulsed operation significantly improves the average and peak power output of the laser [Nishimae and Yoshizawa, 1990, Shahadi et al., 2003]. This improvement is due to the fact that power interruption prevents triggering thermal instabilities and prolongs the vibrational non-equilibrium [Sintov and Shahadi, 2000].

More recently, pulsed microwave experiments have been conducted in CO₂ flows with N₂ admixtures [Silva et al., 2014]. Optical emission spectra from CO and N₂ were used to infer the rotational and vibrational temperature in space and time, where the vibrational temperature of N₂ was used as a proxy for the asymmetric stretch vibrational temperature of CO₂. The vibrational temperature of N₂ was shown to be significantly higher than the rotational or gas temperature ($T_{vib} = 8000$ K vs. $T_{rot} = 900$ K and $T_{gas} = 1100$ K). The vibrational temperature was measured in an electronically excited state, which is not guaranteed to be in vibrational equilibrium with the electronic ground state. Conversion degrees and efficiencies were later determined by measuring the CO concentration using TALIF [Britun et al., 2018]. The conversion degree and efficiency were 23 % and 33 % respectively, and it was concluded that vibrational non-equilibrium played only a minor role under the studied conditions.

To summarize, pulsing microwave power has been used frequently for either diagnostic purposes or to decouple peak and mean power. In the next section we will elaborate on the experimental details of the pulsed microwave setup employed for the experiments described in this paper.

2. Experimental layout

2.1. Reactor

The experiments were performed in the lab of the Elementary Processes in Gas-discharges group at the Eindhoven University of Technology [van de Sande and van der Mullen, 2002, Carbone and Nijdam, 2015, van Gessel et al., 2012] and used their Triple Grating Spectrometer (TGS). The experimental layout is depicted in figure 1. The cell is evacuated by a vacuum pump through a throttle valve which is used to control the pressure be-

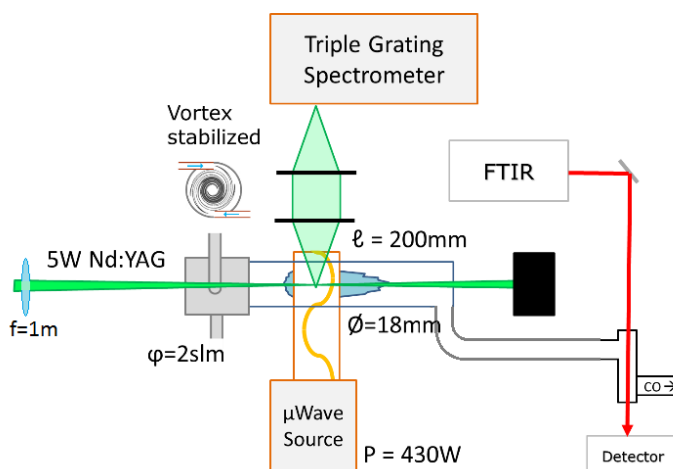


Figure 1: Schematic of the experimental layout. Plasma is produced in the center of the cell with a solid state microwave source. A frequency doubled Nd:YAG laser is focused in the center of the cell. Scattered light is collected with a Triple Grating Spectrometer (TGS). Fourier Transform Infrared (FTIR) absorption spectroscopy is used to determine the exhaust composition.

tween 30 and 160 mbar. The plasma is contained in a 18 mm inner diameter quartz tube with a total length of 20 cm. It is sustained by microwaves produced by a solid state microwave source with a peak power of 430 W that can be modulated with a frequency from DC to 3 MHz and has a variable duty cycle from 0 to 100 %. The microwave power is measured with a 50 dB directional coupler with two thermal sensors attached. All powers reported are absorbed powers, which is the measured forward power minus the reflected power. A mass-flow controller is used to control the gas flow between 1.0 and 5.0 slm. Pure CO_2 gas is tangentially injected to induce a vortex which stabilizes the plasma and prevents contact with the wall. The length of the plasma is typically around 3 cm, but varies for different settings. Similarly, the axial position of the plasma relative to the quartz tube varies for different settings of pressure, power and tuning of the microwave cavity. The processed gas is exhausted through a few meters of bellows that are connected to an FTIR sample cell for composition measurements.

2.2. Diagnostics

A 10 Hz, 4 W frequency doubled Nd:YAG laser is directed axially through the plasma cell equipped with AR-coated windows. A 1 m focal distance lens focuses the beam to the center of the WR340 microwave applicator, where the plasma is produced. The beam diameter at this point is approximately $200 \mu\text{m}$ [van de Sande and van der Mullen, 2002]. The scattered light is collected by two 600 mm focal distance lenses and is imaged onto a triple grating spectrometer with a $250 \mu\text{m}$ slit to filter out the Rayleigh line, which would otherwise obscure the rotational Raman signal [van de Sande and van der Mullen, 2002, Carbone and Nijdam, 2015,

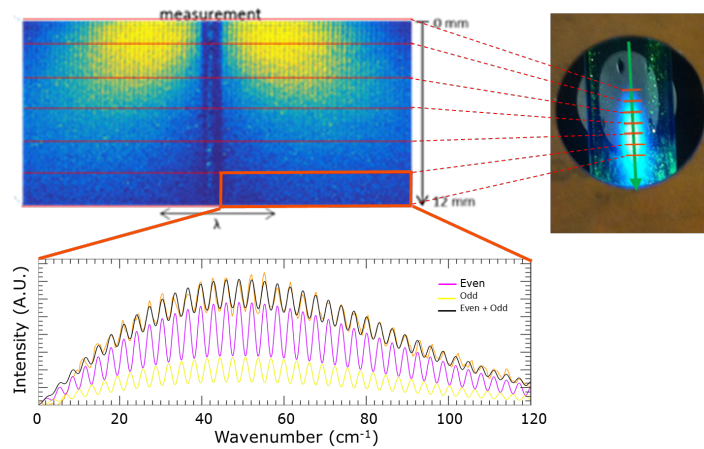


Figure 2: Rotational raman is collected over an axial range of 12 mm. The axial profile is divided and binned over six axial bins. The resulting experimental spectrum is fitted with a synthetic spectrum. Different weights are used for the even and odd component of the rotational spectrum, which are fitted to the data.

van Gessel et al., 2012]. Light is spectrally separated by the first grating and imaged onto a mask of 500 μm to block the Rayleigh line. The light is then combined back into a single beam by the second grating and passed through a slit. The third grating spectrally splits the light again and images the light onto an ICCD camera (Andor iStar 743) that is gated with a gate width of 25 ns. All three gratings have a line density of 1800 mm^{-1} . The spectrum is recorded by integrating 1200 laser shots and is axially binned into 6 axial bins with a total axial coverage of 10 mm. The signal strength in the sixth bin was too low for a reliable fit and has been omitted in the reported temperatures.

The rotational Raman spectrum of CO₂ consists of rotational peaks whose intensity is given by [Brehmer et al., 2014, Herzberg, 1950]:

$$I_J \propto S_J g_n (2J + 1) \exp - \frac{hcF(J)}{kT_{rot}} \quad (1)$$

with S_J the cross-section, g_n the nuclear degeneracy $F(J)$ the rotational energy of rotational level J and T_{rot} the rotational temperature. The nuclear degeneracy in the vibrational ground state is 1 for even and 0 for odd rotational levels. At higher vibrational levels the degeneracy can change, so that both even and odd rotational levels can be visible in the rotational spectrum [van den Bekerom et al., 2018]. To account for the changing degeneracy an apparent degeneracy is used that takes into account the nuclear degeneracy averaged over all vibrational levels. This apparent degeneracy is fitted to the data by using a model with a separate even and odd part:

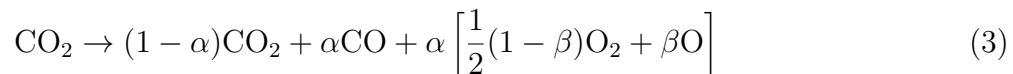
$$I(\nu) = \tilde{g}_e^{fit} I_e(\nu; T_{rot}^{fit}) + \tilde{g}_o^{fit} I_o(\nu; T_{rot}^{fit}) \quad (2)$$

with ν the Raman shift, T_{rot}^{fit} the fitted rotational temperature, I_e and I_o the even and odd part of the rotational spectrum, respectively, and \tilde{g}_e^{fit} and \tilde{g}_o^{fit} the fitted apparent

degeneracy with the restriction that $\tilde{g}_e^{fit} + \tilde{o}_e^{fit} = 1$. Comparing the fitted apparent degeneracy with the apparent degeneracy expected for a thermal gas yields a measure of the vibrational non-equilibrium [van den Bekerom et al., 2018].

Figure 2 depicts the procedure of acquiring, binning and fitting the spectra. The Stokes and anti-Stokes part of the spectrum were fitted separately. The reported temperatures are the mean of the two, with the difference taken as a measure of uncertainty. This difference was typically 15% of the measured rotational temperature or lower. Because of the high rotational relaxation rate [Jacobs et al., 1974], it can be assumed that the rotational temperature is equal to the gas temperature. The fit residue did not indicate any presence of Thomson scattering signal for any of the currently investigated settings.

The effluent gas of the reactor is analyzed by Fourier Transform Infrared (FTIR) absorption spectroscopy to determine overall CO₂ dissociation. A sampling cell is connected in series with the exhaust a couple of meters downstream of the plasma to ensure that the gas has cooled to room temperature and is in chemical equilibrium. This means that all atomic oxygen has reacted away and the effluent consists of only CO₂, CO and O₂. The CO-spectrum is fitted using the HITRAN database and the HAPI routines [Rothman et al., 2013, Kochanov et al., 2016]. Different CO pressure broadening constants are used for the three collision partners, i.e. CO₂, CO (self-broadening) and O₂ [Hartmann et al., 1988, Gamache et al., 2014, Li et al., 2015]. Since O₂ is not IR-active and the CO₂ band is mostly saturated, O₂ and CO₂ densities could not be determined spectroscopically. The conversion degree was therefore determined by the ratio of the CO density to the total density – determined by the pressure and temperature in the cell. The fractions of CO₂ and O₂ in the mixture, necessary to determine the pressure broadening of CO, were calculated using the conversion degree and stoichiometry. The total dissociation reaction is described by:



Here, the CO₂ conversion degree α is given by:

$$\alpha = \frac{2x_{CO}}{2 - (1 + \beta)x_{CO}} \quad (4)$$

where x_{CO} is the CO molar fraction and the O₂ conversion degree β in the sample cell is equal to 0.

A Phantom high-speed CMOS camera is used to measure the phase resolved plasma emission profiles during the plasma pulse, integrated over a spectral range from 350 nm to 1000 nm. The phase of the pulse is defined here as the time delay after the onset of the pulse.

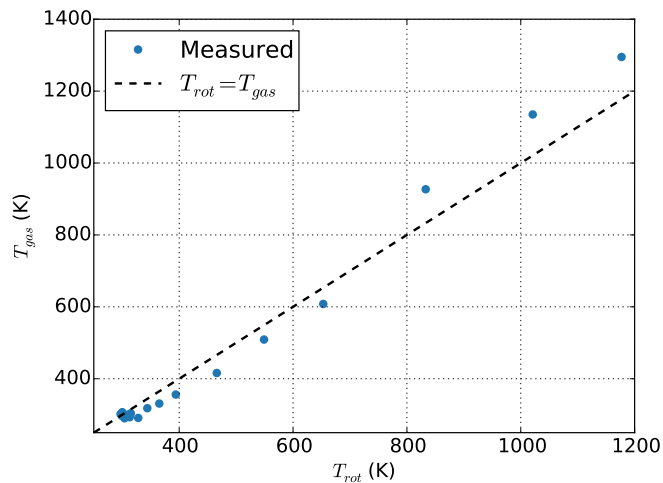


Figure 3: Comparison of temperature obtained by fitting rotational spectrum (horizontal) and by measuring the Rayleigh scattering intensity (vertical). The dashed line indicates $T_{rot} = T_{gas}$

3. Results and discussion

3.1. Rotational temperature as proxy for gas temperature

The rotational temperature obtained from fitting the rotational Raman spectrum is compared to the gas temperature obtained by the Rayleigh intensity. At 100 mbar the rotational relaxation time is in the order of 1 ns [Jacobs et al., 1974], which is significantly faster than the pulsing timescale of $\sim 100 \mu\text{s}$. Rotational and translational temperature are therefore ensured to be in equilibrium, making the rotational temperature a good proxy for the translational (gas) temperature. In 3 the rotational and translational temperatures are compared in an isolated plasma pulse that started at room temperature and is not affected by other pulses. This is necessary to ensure the gas is 100% CO₂ and not contaminated with products. At higher temperatures, the effective cross section is reduced due to product formation [den Harder et al., 2016], leading to an underestimation of the neutral density and overestimation of the temperature.

In places where the two temperatures are dissimilar, the rotational temperature is therefore more reliable because no assumptions have to be made on the composition and the residue can be inspected to assess how well the fitted spectrum matches the measured spectrum. The uncertainty in the fit is increased at higher temperature due to a decreased neutral density.

3.2. Spatio-temporal temperature profiles

The rotational temperature was measured as a function of time delay in a plasma that was modulated at 2.5 kHz and 40% duty cycle, with a mean power of 150 W.

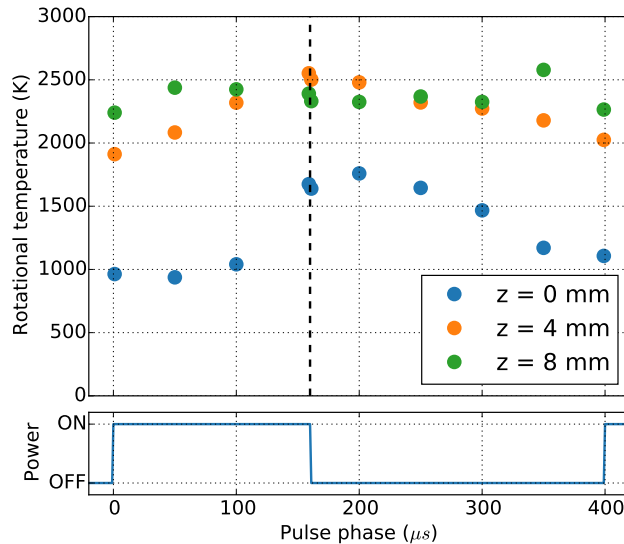
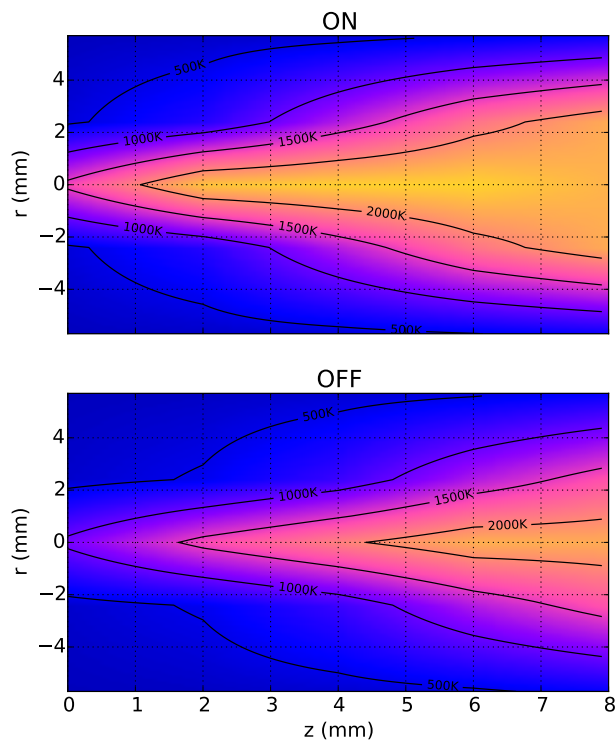


Figure 4: Phase resolved temperature measurement for different axial coordinates. Upstream ($z = 0$), the temperature is significantly lowered during the OFF-time. Further downstream ($z = 4$ & 8 mm), power modulation has little influence on the temperature. Conditions: $f = 2.5$ kHz, $\eta_{DC} = 40\%$, $P_{mean} = 150$ W, $p = 75$ mbar, $\varphi = 1.9$ slm.

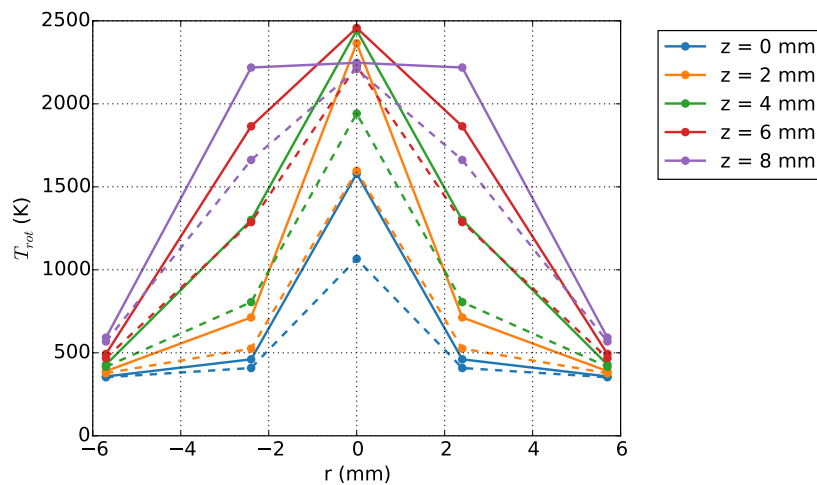
The pressure was 75 mbar at a flow rate of 1.9 slm. The results are plotted in figure 4. The temperature difference between ON- and OFF time is largest at the axial start of the plasma ($z = 0$ mm), which is roughly 800 K. Further downstream, the difference is less pronounced and at 8 mm there is no clear correlation between the temperature evolution and power modulation. The temperature peaks at 2500 K. Under the assumption of plug-flow the gas was displaced 4 mm in the 240 μ s OFF time, which is roughly 10% of the total plasma length. Thus displacement of gas can account for roughly a 10% decrease in temperature, which is consistent with measurements. Although the temperature is significantly lower after the plasma OFF-time, it does not go below 1000 K, a temperature at which vibrational quenching is still expected to be an important relaxation mechanism.

A radial temperature profile was measured by translating the cell in the fixed beam path for two sets of conditions. One was at 75 mbar, 1.9 slm, 2.5 kHz, 40% duty cycle, and 150 W mean power – identical to the parameter settings for the time-evolution measurement presented in figure 4. The other was at 160 mbar, 1.9 slm, 5 kHz, 50% duty cycle, and 80 W mean power, which are the same settings used in the next section (section 3.3). The axial temperature profile was measured for t_{ON} and t_{OFF} at three radial positions: 0, 2.5, and 6 mm from the center. These 3×5 data points were linearly interpolated and mirrored across the axial axis to obtain 2D profiles shown in figures 5 and 6, corresponding to the two datasets respectively.

The temperature of the 75 mbar and 150 W plasma peaks at 2950 K during the

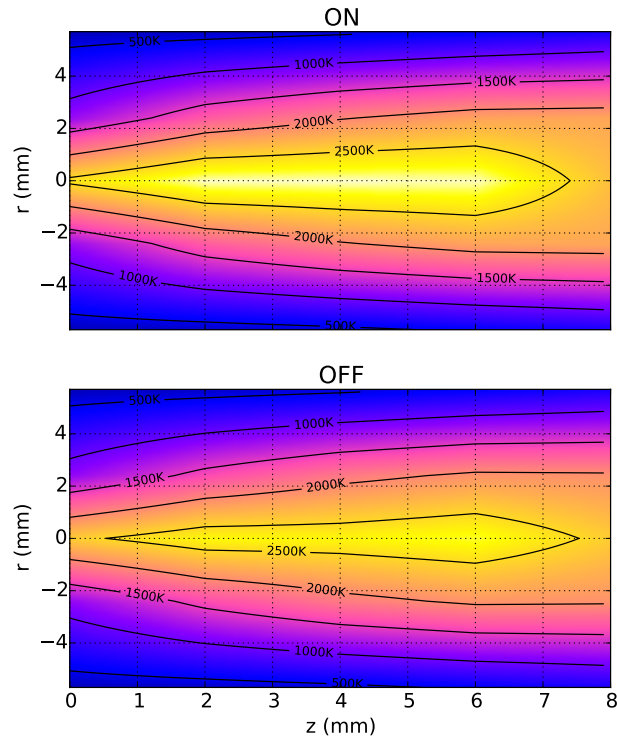


(a) Contour plot

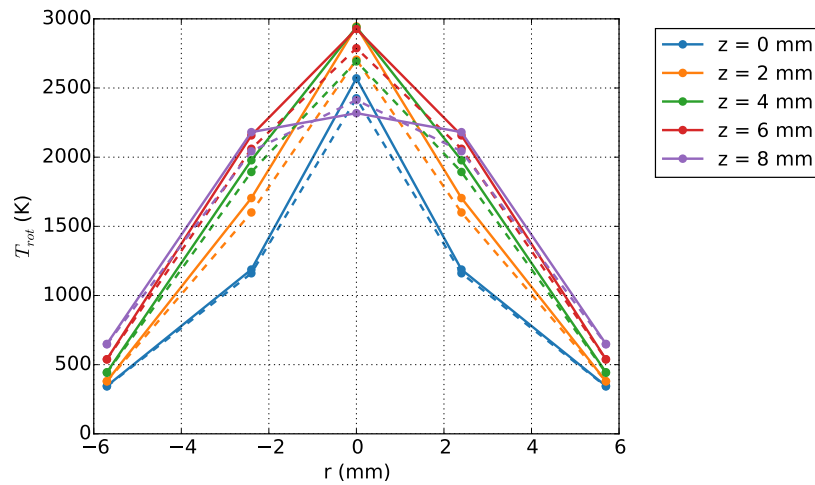


(b) Radial cross sections

Figure 5: (a) Contour plot of measured rotational temperature profile after $160 \mu\text{s}$ of power ON (upper) and after $240 \mu\text{s}$ of power OFF (lower). Conditions: $f = 2.5 \text{ kHz}$, $\eta_{DC} = 40\%$, $P_{mean} = 150 \text{ W}$, $p = 75 \text{ mbar}$, $\varphi = 1.9 \text{ slm}$. (b) Radial cross sections of same data. Data was only measured for one radial arm ($r \geq 0$) and mirrored for visibility.



(a) Contour plot



(b) Radial cross sections

Figure 6: (a) Contour plot of measured rotational temperature profile during after 100 μ s of power ON (upper) and after 100 μ s of power OFF (lower). Conditions: $f = 5.0$ kHz, $\eta_{DC} = 50\%$, $P_{mean} = 80$ W, $p = 160$ mbar, $\varphi = 1.9$ slm. (b) Radial cross sections of same data. Data was only measured for one radial arm ($r \geq 0$) and mirrored for visibility.

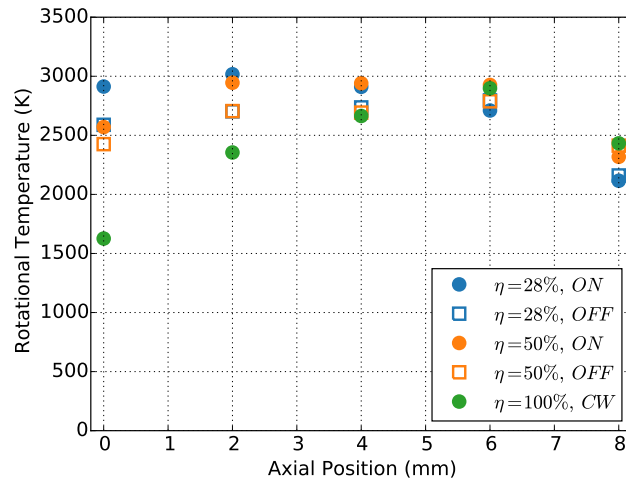


Figure 7: Axial temperature profiles for different duty cycles at constant mean power. At higher peak power, the peak temperature increases slightly and the axial profile flattens. Conditions: $f = 5.0 \text{ kHz}$, $\eta_{DC} = \text{varied}$, $P_{mean} = 80 \text{ W}$, $p = 160 \text{ mbar}$, $\varphi = 1.9 \text{ slm}$.

ON-time at $240 \mu\text{s}$ and the temperature reduces to 2400 K in the OFF time at $400 \mu\text{s}$. Like before, the gas is displaced by 4 mm during the OFF time, which is visible by comparing top and bottom diagram. An important finding is that the edges of the plasma remain relatively cold. In figure 6, temperatures of the plasma at 160 mbar and 80 W are depicted. The peak temperatures are significantly higher even though the power input is lower. This is likely a result of slower displacement than at 75 mbar , because the flow velocity dz/dt in a plug flow reactor at constant pressure is reduced at higher pressure p_0 (see eq. 10), and a smaller plasma volume leading to peaking of the power density profile. Under these conditions, the wall temperature also remains low, even if the core temperature is much higher.

3.3. Influence of peak power and pressure on gas temperature

The mean power was kept constant so that temperatures and efficiencies of pulsed and continuous power plasmas can be directly compared. In changing the duty cycle at constant mean power, inevitably the pulsing frequency is also changed, changing the plasma ‘ON’- and ‘OFF’-times. Axial temperature profiles were measured for a variety of settings with pressures of 30 mbar , 85 mbar , and 160 mbar at flows of $1.9 - 5.0 \text{ slm}$, at a mean power of 80 W and frequency of 2.5 to 5.0 kHz . Unlike magnetron sources, the solid state source used in this experiment remains stable over the full range and allows stable plasma operation at much lower power.

The measured axial temperature profiles were similar in each case: A flat axial profile is observed with a peak temperature that is the same for all discharges with a given pressure. A typical profile is presented in figure 7. The value of the peak

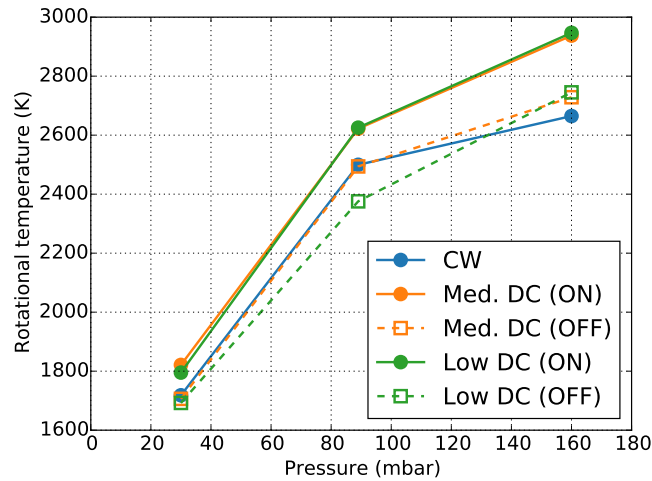


Figure 8: Highest temperature along the axial coordinate after the “ON” and “OFF” times of the pulse for different pressures. Duty cycles vary from discharge to discharge for stability considerations. ‘Low’ duty cycles are 20 % to 30 %, ‘Medium’ duty cycles are 45 % to 50 %. Conditions: $f = 5.0$ kHz, $\eta_{DC} = \text{varied}$, $P_{\text{mean}} = 80$ W, $p = \text{varied}$, $\varphi = 1.9$ slm.

temperature is strongly correlated with pressure, with lower peak temperatures at lower pressures, as shown in figure 8. This pressure dependence can be explained by the changing plasma volume (see section 3.4): The larger plasma volume at lower pressures results in a lower volumetric power density, which in turn results in lower peak temperatures.

CO production was measured with FTIR for the duty cycle scans at 1.9slm and constant mean power of 80 W. Figure 9 depicts the measured CO production as a function of duty cycle and pressure. There are two clear trends to be observed in this figure: Firstly, the energy efficiency significantly increases with higher pressure. This can likely be attributed to the increased temperatures at higher pressures that were shown in figure 8. Secondly, reducing the duty cycle at the same mean power implies increasing the peak power. It is observed that at lower duty cycles, i.e. higher peak powers, the efficiency is improved further. This is consistent with the increased peak power inducing higher peak temperatures, as was observed in figure 7. This explanation is explored further in section 3.5 where a thermal kinetics model is developed to support these results. At too low duty cycles, the plasma input power might be applied too briefly to reach the high steady state temperature, resulting in a lower efficiency as indicated by the lower efficiency at 20 % duty cycle and 160 mbar in figure 9.

3.4. Plasma emission

Plasma emission was recorded as a function of time for three duty cycles 100%(CW), 50 % and 20 % at a frequency of $f = 5.0$ kHz, mean power of $P_{\text{mean}} = 80$ W, pressured of

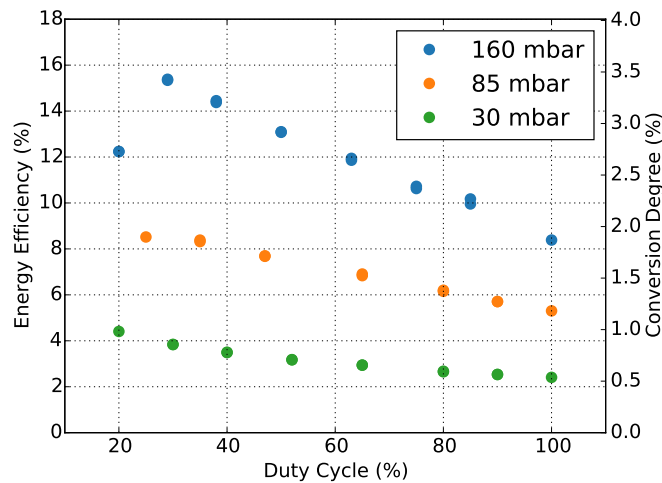


Figure 9: Energy efficiency and conversion degree as a function of duty cycle at constant mean power of 80 W for three different pressures. Energy efficiency increases with pressure and peak power. Because the average SEI is the same for every datapoint, energy efficiency and conversion degree have a linear relationship. Conditions: $f = 5.0$ kHz, $\eta_{DC} = \text{varied}$, $P_{\text{mean}} = 80$ W, $p = \text{varied}$, $\varphi = 1.9$ slm.

30, 90, and 160 mbar, and a flowrate of $\varphi = 2.9$ slm. High speed images were recorded with an acquisition time of $10 \mu\text{s}$ and were used to determine the radius and length of the plasma for different pressures and duty cycles at a constant mean power of 80 W. The plasma shape does not appear to change during the pulses, indicating that all onset effects are stabilized within a single frame of $10 \mu\text{s}$. The shape does change for different pressures, as both the plasma width and length are observed to decrease with increasing pressure, shown in figure 10. At higher peak powers, the plasma both contracts and elongates. The contraction is explained by the increased electron density at higher peak power, which reduces the skin depth of the microwaves [den Harder et al., 2016]. Due to the high electron density at high power, evanescent waves can propagate along the surface of the plasma, elongating the discharge.

3.5. Thermal kinetics model

Qualitatively, the effect of power pulsing can be understood in a thermal framework by considering the different power loss mechanisms in the plasma. Here, we distinguish transport and chemistry. The advection of heat from the hot core to the cold edge is determined by the temperature gradient, which is linear with the core temperature. Chemical reactions have an exponential temperature dependence (see eq 6). At (quasi-) steady state, the input power is balanced by the power loss:

$$P_{in} = C_L(T - T_0) + C_E \exp\left[-\frac{E_a}{kT}\right] \quad (5)$$

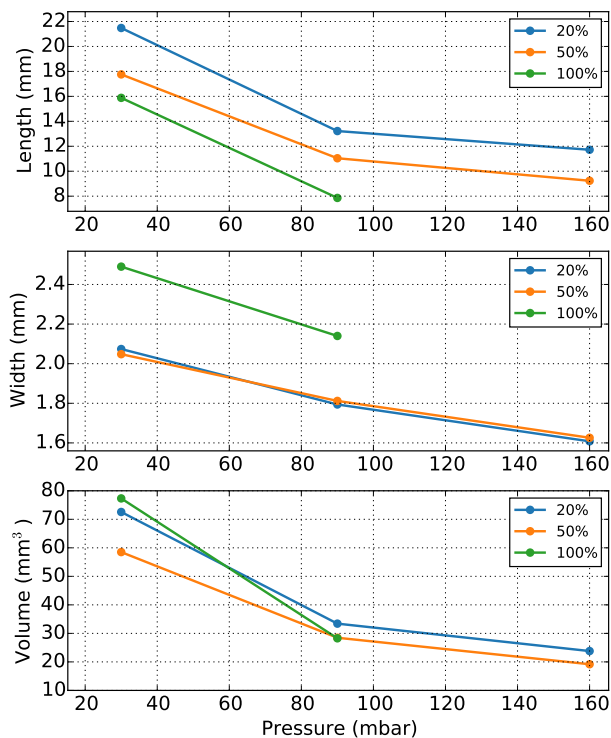


Figure 10: The FWHM length and width of the plasma in pixels as a function of pressure for different duty cycles at constant mean power. The width and length increase with reduced pressure. Volume is calculated as $V = 0.25\pi Lw^2$. Conditions: $f = 5.0$ kHz, $\eta_{DC} = \text{varied}$, $P_{\text{mean}} = 80$ W, $p = \text{varied}$, $\varphi = 2.9$ slm.

At temperatures at which thermal chemistry is not yet activated, all power will be lost by radial transport. If the gas reaches higher temperatures, chemistry will be activated and part of the power will be channeled into dissociation reactions. The higher the input power, the larger the power fraction that is channeled into dissociation, as depicted schematically in figure 11. Note that because of the exponential dependence, at this point the temperature rises only very little even if a large power is applied. This explains why the peak temperatures were all similar; once the chemical channel is accessible power will be deposited in dissociation and temperature will not rise much. This also means that chemical equilibration times play a role.

In the rest of this section, a simple 0D thermal kinetics model is evaluated to qualitatively explain the increase in conversion at higher peak powers. The aim is to make a minimal model that only includes features necessary to test if the observed behaviour can be explained by thermal chemistry. For simplicity, we ignore contributions of direct electron impact, which in practice may have a non-zero contribution.

The model describes a plug-flow reactor and assumes a test volume travelling through the plasma volume, which is modeled as a volume that supplies heat to the test volume with a homogeneous power density. It is assumed that the only function

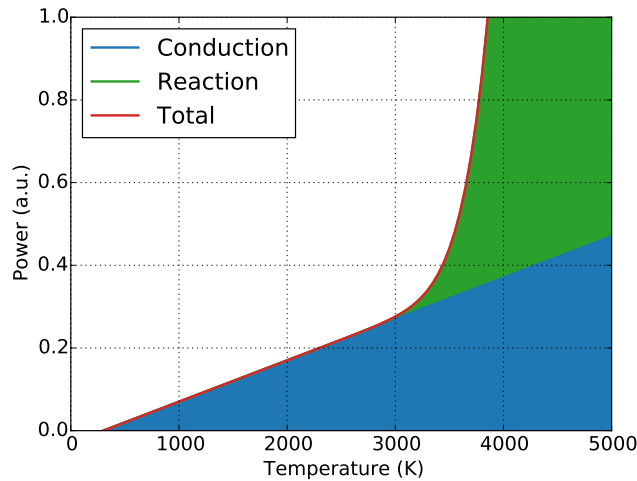


Figure 11: The power that must be invested to increase the temperature to some value.

of the plasma is to heat the volume. Each iteration consists of two steps. In the first step, the molecules will react, changing the composition and adding or removing heat. In second step, the reaction heat together with heat added by the plasma increase the gas temperature in the test volume.

In total 16 reactions are included, which are 8 pairs of balanced reactions involving the species CO₂, CO, O₂ and O. The rate constants that were used are the same as the ones by Den Harder [den Harder et al., 2016, Butylkin et al., 1979]. The reaction rate $k_i(T)$ of reaction i at a temperature T is given by:

$$k_i(T) = k_{0,i} \exp \left[-\frac{E_{a,i}}{k_B T} \right] \quad (6)$$

For each of the 16 reactions, the rate coefficient $k_{0,i}$ and activation energy $E_{a,i}$ are given in table 1. The rate coefficients are used for calculating the reaction rate. As an example, the change in CO density as a result of reaction 1 is:

$$dn_{CO,1} = k_1(T)n_{CO_2}^2 dt \quad (7)$$

The total change in density per step for each species is obtained by summing the rate equations like eq. 7 over all reactions. Because of the reactions, the flow rate has changed as a result of produced or destroyed particles in the test volume:

$$d\phi = \phi \frac{k_B T}{p} \sum_j dn_j \quad (8)$$

with ϕ the molecular flow rate in s⁻¹. Molecules can produce or consume heat in the reaction. The heat added to the test volume each iteration is equal to the heat absorbed from the plasma minus the heat consumed in the reaction:

$$dT = \frac{u_0 dt - \sum_j H_j(T) dn_j}{\sum_j C_{p,j}(T) n_j} \quad (9)$$

Table 1: Reaction rate constants and activation energies for the 16 reactions included in the thermal kinetics model. The bottom 8 reactions are the reverse reactions of the first 8. Reaction rate constants are in units of m³s⁻¹ for binary reactions or m⁶s⁻¹ for ternary reactions [den Harder et al., 2016].

Index	Reaction	k_0	E_a (eV)
1	$\text{CO}_2 + \text{CO}_2 \longrightarrow \text{CO} + \text{O} + \text{CO}_2$	4.38×10^{-13}	5.58
2	$\text{CO}_2 + \text{CO} \longrightarrow \text{CO} + \text{O} + \text{CO}$	4.38×10^{-13}	5.58
3	$\text{CO}_2 + \text{O}_2 \longrightarrow \text{CO} + \text{O} + \text{O}_2$	3.72×10^{-16}	5.19
4	$\text{CO}_2 + \text{O} \longrightarrow \text{CO} + \text{O}_2$	7.77×10^{-18}	1.57
5	$\text{O}_2 + \text{O}_2 \longrightarrow \text{O} + \text{O} + \text{O}_2$	8.14×10^{-15}	5.14
6	$\text{O}_2 + \text{O} \longrightarrow \text{O} + \text{O} + \text{O}$	1.99×10^{-14}	4.98
7	$\text{O}_2 + \text{CO} \longrightarrow \text{O} + \text{O} + \text{CO}$	2.41×10^{-15}	5.12
8	$\text{O}_2 + \text{CO}_2 \longrightarrow \text{O} + \text{O} + \text{CO}_2$	2.57×10^{-15}	5.14
9	$\text{CO} + \text{O} + \text{CO}_2 \longrightarrow \text{CO}_2 + \text{CO}_2$	6.54×10^{-45}	0.19
10	$\text{CO} + \text{O} + \text{CO} \longrightarrow \text{CO}_2 + \text{CO}$	6.54×10^{-45}	0.19
11	$\text{CO} + \text{O} + \text{O}_2 \longrightarrow \text{CO}_2 + \text{O}_2$	6.51×10^{-48}	-0.16
12	$\text{CO} + \text{O}_2 \longrightarrow \text{CO}_2 + \text{O}$	1.23×10^{-18}	1.32
13	$\text{O} + \text{O} + \text{O}_2 \longrightarrow \text{O}_2 + \text{O}_2$	6.81×10^{-46}	0.00
14	$\text{O} + \text{O} + \text{O} \longrightarrow \text{O}_2 + \text{O}$	2.19×10^{-45}	-0.20
15	$\text{O} + \text{O} + \text{CO} \longrightarrow \text{O}_2 + \text{CO}$	2.76×10^{-46}	0.00
16	$\text{O} + \text{O} + \text{CO}_2 \longrightarrow \text{O}_2 + \text{CO}_2$	2.76×10^{-46}	0.00

where u_0 is the applied volumetric power density in Wm⁻³, dt the timestep, $C_{p,j}$ is the heat capacity, $H_j(T)$ the enthalpy including the enthalpy of formation, and dn_j the change in number density of species j . The axial position of the test volume is determined by integrating the velocity:

$$dz = \frac{\phi k_B T}{p_0 A} dt \quad (10)$$

At the end of every iteration, n_j , ϕ , T and z are updated to their new values. The new densities n_j are then re-normalized to ensure that $\sum_j n_j = p/kT$. This, together with eq. 8 implements the assumption of constant pressure in the reactor.

In practice the plasma is far from a homogeneous heating source; it consists of a high temperature core surrounded by a comparatively cold shell, as was observed in figures 5 and 6. To model this behaviour more accurately, we distinguish two volumes. The first volume, the core, is directly heated by the plasma as described above. The second volume, the shell, is not directly heated by the plasma but is diffusively heated by the core volume, described by following equation:

$$\frac{dQ}{dt} = -k_{eff} A_{cs} \frac{T_{core} - T_{shell}}{\Delta r} \quad (11)$$

conversely, the core volume is cooled by the shell. $\frac{dQ}{dt}$ is the power deposited in the shell, A_{cs} the cross-sectional area, T_{core} and T_{shell} the temperatures in the core and

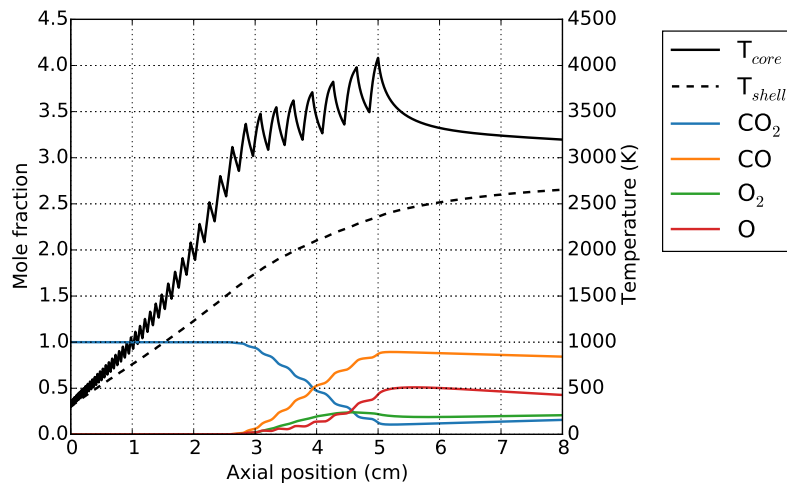


Figure 12: Evolution of composition and temperature of the core and shell for a simulated pressure of 100 mbar at a flow of 2 slm, mean power of 100 W, pressure of 100 mbar and pulse frequency of 5 kHz at 50 % duty cycle. The composition is in molar fraction of the initial composition. The solid black curve indicates the temperature in the core, the dashed black curve the temperature in the edge. The composition only changes when the temperature increases above some threshold.

shell volumes respectively, and k_{eff} is the effective heat conductivity between the two volumes and Δr the separation distance between the two volumes. In this model, we have not taken into account electron impact dissociation, which could be a significant source of dissociation.

It is evident that this simple model overlooks some important features of the real discharge like convective flow, particle mixing and turbulence. Ultimately, these mechanisms help to transfer energy from the core to the edge, so they can be taken into account by assuming a larger value for k_{eff} . We emphasize here that the aim is only to develop a simple model that can explain qualitative features of the plasma.

Figure 12 depicts the evolution of temperature and composition for a simulation with pressure of 100 mbar, 2 slm flow, 100 W mean power, and pulse frequency of 5 kHz at 50 % duty cycle. At low temperatures, the composition does not change because chemical reactions are not activated yet. As soon as the temperature gets above the threshold of 3000 K, CO starts to form. During a power pulse, clearly the conversion momentarily increases as the temperatures is raised. The temperature in the shell is too low for significant conversion.

This 0D-model was used to calculate the thermodynamic efficiency for different duty cycles while keeping constant mean power of 80 W. Energy efficiency was evaluated at transport coefficients $k_{eff}/\Delta r$ (eq 11) of $1.5 \times 10^4 \text{ Wm}^{-2}\text{K}^{-1}$ and $2.0 \times 10^4 \text{ Wm}^{-2}\text{K}^{-1}$. These values were chosen to maximize the qualitative effect in the model, rather than trying to match them to experimental values. The thermal conductivity of the

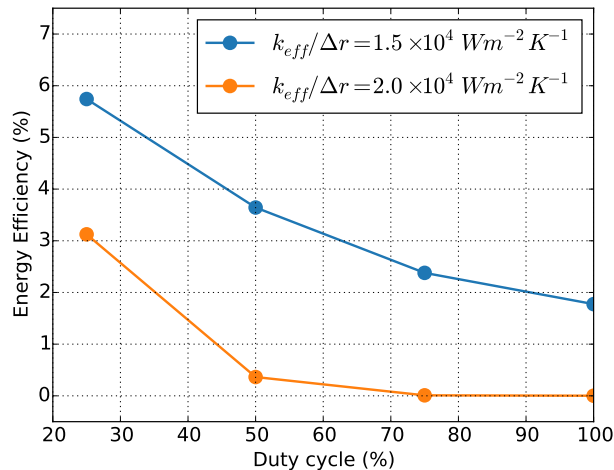


Figure 13: Simulated efficiency for a core plasma of 2.5 mm for different duty cycles at constant mean power of 80 W. At lower duty cycles, the higher peak power results in higher temperatures which drive chemistry more efficiently.

mixture was calculated using the NASA CEA program [Gordon and McBride, 1994, McBride and Gordon, 1996, Svehla, 1995]. A mixture of CO₂, CO, O₂ and O at thermal equilibrium at a temperature of 3000 K and pressure of 160 mbar has a thermal conductivity of $1.4 \text{ Wm}^{-1} \text{ K}^{-1}$. If we further assume the length of the temperature gradient to be 5 mm, this leads to a value of $k/\Delta r$ of $280 \text{ Wm}^{-2} \text{ K}^{-1}$. Though this number is two orders of magnitude smaller than the values used in simulation, we note it only includes diffusive heat transport. In practice convection will have a large contribution to the thermal conductivity.

At $k_{eff}/\Delta r = 2.0 \times 10^4 \text{ Wm}^{-2} \text{ K}^{-1}$ the effect of increased peak power becomes only noticeable at high peak powers, depicted in figure 13. This is because the transport cools the core so much that it does not get hot enough to enable chemistry. At $k_{eff}/\Delta r = 1.5 \times 10^4 \text{ Wm}^{-2} \text{ K}^{-1}$ the core is better insulated and the threshold temperature for chemical activation is reached. Once the temperature is above the threshold, increasing the peak power increases the fraction of power used for conversion as shown in figure 11. Because the average SEI does not change, an increase in conversion directly translates to an increase in energy efficiency.

3.6. Effect of inhomogeneous heating on thermal efficiency

Since CO₂ microwave plasmas have been shown to reach very high temperatures [den Harder et al., 2016], thermal conversion likely has a significant contribution to the total dissociation. We will therefore assess to what extent plasma effects (e.g. electron impact dissociation or vibrational non-equilibrium) have a role in efficient plasma dissociation and how much can be attributed to thermal conversion. In this section, we will explore under what conditions a plasma can outperform thermal conversion.

The main point of this section is to demonstrate that by considering inhomogeneous heating, only few plasma reactors reported in literature outperform the best possible thermal efficiency.

In thermal equilibrium, the energy input and composition both are a function of temperature. At a given temperature, the energy efficiency is therefore also known. For practical use of the products, the gas must cool down to room temperature first. During the cooling down phase, produced CO may react back to CO₂, degrading the overall energy efficiency. The efficiency values obtained at a given temperature are therefore only valid under the “ideal quenching” assumption, where the gas cools down so fast that back reactions are negligible. The efficiency values calculated here are based on the energy that ends up in the CO molecule. It is thus assumed that atomic oxygen does not react with CO₂ to form more CO, but instead the oxygen reacts back via $2O \rightarrow O_2$. This directly relates the energy efficiency η to the CO₂ dissociation degree α :

$$\eta = \frac{\Delta H}{SEI} \alpha \quad (12)$$

with ΔH the reaction enthalpy of 2.93 eV per molecule [Chase, 1998] and the Specific Energy Input (SEI) the invested energy per molecule, which for a system in thermal equilibrium is defined here as:

$$SEI = \frac{\sum_j N_j(T) H_j(T)}{N_0} - H_{CO_2}(298K) \quad (13)$$

here $N_j(T)$ is the number of molecules of species j (CO₂, CO, O₂ and O) in an enclosed but expandable volume at temperature T and a constant pressure of 100 mbar, N_0 is the number of molecules in the volume at room temperature (298 K), and $H_j(T)$ is the enthalpy of species j at temperature T including the enthalpy of formation. Since the enthalpy is referenced to $T = 298$ K, $H_{CO_2}(298K)$ is just the enthalpy of formation of CO₂. The SEI, the conversion degree, and energy efficiency are a function of temperature in thermal equilibrium. In figure 14, conversion and energy efficiency for thermal conversion are plotted versus the SEI and compared to results from plasma experiments in literature.

Thermal conversion is first considered the case where the entire volume is heated homogeneously. For homogeneous heating the entire volume is assumed to have the same temperature. Conversion degree and energy efficiency for homogeneous heating as function of SEI are depicted by the blue lines in figure 14. Both the conversion degree and energy efficiency have a theoretical limit, indicated by the orange line. The conversion is limited at low SEI when the available energy is insufficient to dissociate all molecules. The energy efficiency is limited at high SEI when the energy input exceeds the energy ΔH necessary for complete dissociation.

For homogeneous heating, it was assumed that the entire volume is heated to the same temperature. In practice, it is likely that not all gas has the same temperature. It is known for example that the contracted regime has a strongly localized power deposition profile. We will therefore look at the case where heating is *inhomogeneous*. We consider the simple case of a volume of which only a fraction x is heated, depicted

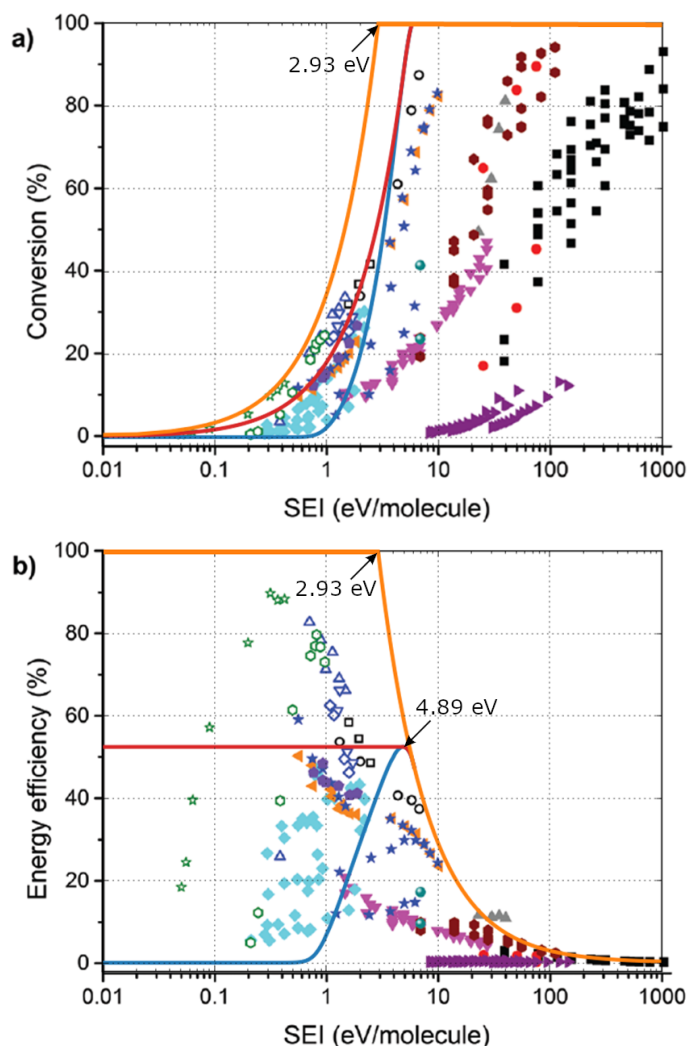


Figure 14: Conversion (a) and energy efficiency (b) for a collection of microwave discharges vs the Specific Energy Input (SEI). The orange line depicts the theoretical maximum conversion and energy efficiency, respectively, the blue line depicts the thermal conversion and energy efficiency for homogeneous heating, the red line indicates inhomogeneous heating. Data is taken from [Snoeckx et al., 2015]

in figure 15. Because there is now a distinction between the heated and non-heated volume, a distinction between average SEI and local SEI must be made. The local SEI is the SEI considering only the heated part of the volume. At a fixed average SEI, the local SEI will increase for a smaller heated fraction x , as depicted in figure 15. The local SEI is given by:

$$SEI_{loc} = \frac{SEI_{avg}}{x} \quad (14)$$

In figure 16, the local SEI vs the heated fraction is plotted for three different average SEI. The black dashed line indicates the SEI at which thermodynamical conversion has the maximum energy efficiency. The plot shows that as long as the average SEI is lower

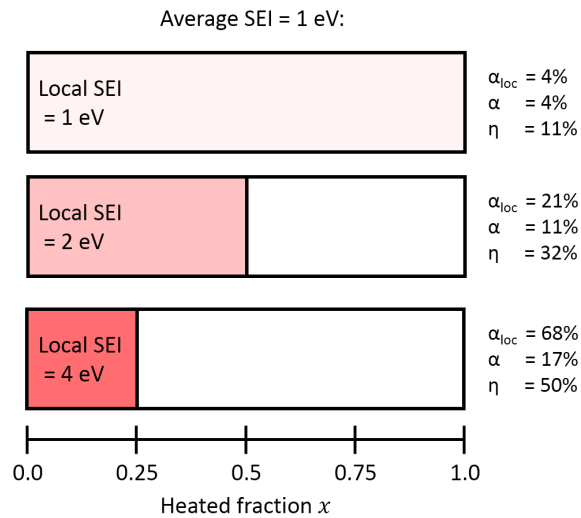


Figure 15: Inhomogeneous heating can increase the local SEI at a fixed average SEI. In this way, improved energy efficiency of thermodynamical conversion is possible.

than the SEI at which thermal conversion is most efficient ($SEI_{\eta_{max}} = 4.89$ eV), reducing the heated fraction x can increase the local SEI and improve the efficiency. In short, this means that for any average SEI below 4.89 eV, the maximal thermodynamic efficiency can be reached. In this discussion we neglect any thermal gradients and assume the processed gas consists of gas at two different temperatures.

When the average SEI is too high, inhomogeneous heating cannot improve efficiency since lowering the heated fraction can only increase the local SEI. This is observed in figure 16 by the green line not intersecting with the dashed black line. The value of $SEI_{\eta_{max}}$ must not be confused with the reaction enthalpy $\Delta H = 2.93$ eV, at which uniquely a theoretical 100 % conversion at 100 % efficiency can be reached.

While the energy efficiency can be optimized to the thermodynamical maximum by reducing the heated fraction, the conversion in an inhomogeneously heated volume will be smaller than a homogeneously heated volume with the same local SEI, simply because a smaller volume is taking part in the conversion. The conversion for an inhomogeneously heated volume is given by:

$$\alpha = x\alpha_{loc} = x \frac{SEI_{loc}}{\Delta H} \eta \quad (15)$$

The thermodynamical conversion and energy efficiency for inhomogeneously heated gas is plotted in red in figure 14. Notably, the amount of datapoints that can be described by thermodynamical conversion significantly increased by including inhomogeneous heating. An additional result is that in comparing plasma to thermodynamical dissociation, only the energy efficiencies have to be compared.

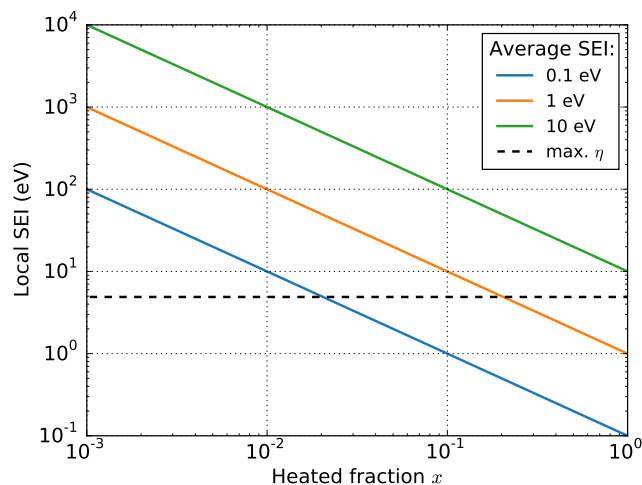


Figure 16: The local SEI increases is plotted as a function of heating fraction x at three values of average SEI. When $SEI_{avg} < SEI_{\eta_{max}}$, a heating fraction can be found at which SEI_{loc} is optimal for thermodynamic efficiency (indicated by the black dashed curve).

4. Possible contribution of vibrational excitation

Extrapolating from the present work, it is expected that thermal conversion had a significantly larger contribution to dissociation than has been recognized in the early plasma dissociation experiments [Fridman, 2008, Vakar et al., 1981, Legasov et al., 1978, Asisov et al., 1981, Asisov et al., 1983]. We therefore conclude that vibrational non-equilibrium is generally not the leading mechanism at play in microwave CO_2 plasma. In this section we will speculate about how the efficiencies observed in the 80's may still have been achieved.

The strongly peaked radial temperature profile suggest that there are two distinct regions in the plasma: a cold edge and a hot core. This separation is probably stronger due to tangential gas injection resulting in a swirl flow. It is textbook knowledge that for such flow profiles recirculation zones may appear. A recirculation zone is a flow field with closed flow lines, where gas can only enter or exit by diffusion. The closed flow lines act form a transport-barrier that drives a steeper temperature gradient.

In the view of the two separate zones, only the hot core is heated by microwave power. As this region is confined by closed flow lines, power can leave the volume only by diffusion of either hot CO_2 or products. The core temperature will rapidly increase until an equilibrium between input power and diffusion is reached. The equilibration of input power and diffusion of products would explain why core temperatures at which thermal chemistry becomes important are so ubiquitous.

Gas that diffuses out of the hot core will end up in the stream of cold gas in the edge region. The strong temperature gradient between the core and edge promotes

fast quenching, causing the high temperature composition to remain largely intact and prevent back-reactions.

Above 3500 K, the temperatures reported by Den Harder [den Harder et al., 2016], oxygen exists mostly in its atomic form. If quenching is fast enough, the atomic oxygen will survive and end up in the cold gas stream. Atomic oxygen, being a radical, can still be very reactive. Oxygen can react with vibrationally excited CO₂ to form additional CO and increase the overall efficiency. The concept of atomic oxygen reacting with CO₂ during quenching is termed super-ideal quenching.

In addition to CO and O, hot CO₂ may also diffuse out of the core. The CO₂ is carrying a significant amount of stored energy in its vibrational manifold. While translational energy is lost rapidly in the presence of cold gas, loss of vibrational excitation relies on VT-relaxation which is a couple of orders slower than VV-relaxation. A vibrational non-equilibrium would thus arise due to highly energetic CO₂ mixing with cold gas rather than by preferential electron energy transfer. The highly vibrational excitation provides the necessary energy for dissociation reactions by atomic oxygen.

We note that in the above description, the majority of the dynamics are governed by high temperature kinetics. While the role of vibrational excitation in this picture is only minor, this description seems more compatible with experimental results reported in this paper.

A consequence of the paradigm presented here is that the research interest should shift from the core – which would be in thermal equilibrium at a high temperature – to the intermediate region where the core and edge meet. The main question becomes how effective the edge layer is in quenching the products exiting the hot core. Measuring the composition and temperatures in the intermediate region would be the first step in quantifying these effects.

5. Conclusions

The importance of thermal conversion in the dissociation of CO₂ in a microwave discharge was assessed by measuring the temporally and spatially resolved temperature while pulsing the power. Temperature evolution of pulsed microwave plasma was studied at various conditions. Generally, we find that the cooling of the plasma in between pulses is limited, and temperature remains sufficiently high that substantial vibrational excitation is not likely to persist.

The edge remained cold, on the order of 500 K while core temperatures of up to 3000 K have been measured. This high thermal gradient is essential in increasing the thermodynamical efficiency by thermally quenching the reactive mixture and preventing thermal back reactions.

Axial profiles of the rotational temperature were measured by rotational Raman scattering. The peak temperature was shown to increase strongly with pressure. This is attributed to the fact that the plasma volume decreases for higher pressure, increasing the spatial power density. The duty cycle of the pulsed microwave was scanned in order

to vary the power density without changing the mean power. The energy efficiency was found to increase for higher pressures and shorter duty cycles, which can be explained by the fact that in both cases the power density is increased.

The high power density results in a high temperature in the gas, which is necessary for efficient thermal conversion. This is explained as a competition between transport and chemistry; at high temperatures, the fraction of power that goes into reactions is increased exponentially. This was verified in a simple numerical model. Plasma performance of plasma reported in literature was compared with thermodynamic conversion efficiency. By considering that plasmas heating can be inhomogeneous, we have shown that the parameter space at which thermal conversion is efficient can be extended significantly.

In conclusion, the CO₂ dissociation in the microwave plasma can be explained by thermal conversion to a satisfactory degree. Nevertheless, shaping the power density in the reactor by e.g. pulsing the power, higher local temperatures can be reached which increases the thermodynamical efficiency.

6. References

- [Ageeva et al., 1986] Ageeva, N. P., Novikov, G. I., Raddatis, V. K., Rusanov, V. D., and Fridman, A. (1986). *Sov. Phys., High Energy Phys.*, 20:284.
- [Asisov et al., 1981] Asisov, R., Givotov., V., Krashennnikov, E., Krotov, M., Potapkin, B., Rusanov, V., and Fridman, A. (1981). *5th International Symposium on Plasma Chemistry, Edinburgh*, 1:52.
- [Asisov et al., 1983] Asisov, R., Givotov., V., Krashennnikov, E., Potapkin, B., Rusanov, V., and Fridman, A. (1983). *Sov. Phys., Doklady*, 271:94–98.
- [Baeva et al., 2001] Baeva, M., Gier, H., Pott, A., Uhlenbusch, J., Hschele, J., and Steinwandel, J. (2001). Studies on Gas Purification by a Pulsed Microwave Discharge at 2.46 GHz in Mixtures of N₂/NO/O₂ at Atmospheric Pressure. *Plasma Chemistry and Plasma Processing*, 21.
- [Bongers et al., 2016] Bongers, W. A., Bouwmeester, H., Wolf, A. J., Peeters, F. J. J., Welzel, S., van den Bekerom, D. C. M., den Harder, N., Goede, A. P. H., Graswinckel, M. F., Groen, P. W., Kopecki, J., Leins, M., van Rooij, G., Schulz, A., Walker, M., and van de Sanden, M. C. M. (2016). Plasma-driven dissociation of CO₂ for fuel synthesis. *Plasma Process. Polym.*, 14.
- [Brehmer et al., 2014] Brehmer, F., Welzel, S., van de Sanden, M. C. M., and Engeln, R. (2014). CO and byproduct formation during CO₂ reduction in dielectric barrier discharges. *J. Appl. Phys.*, 116.
- [Britun et al., 2018] Britun, N., Silva, T., Chen, G., Godfroid, T., van der Mullen, J., and Snyders, R. (2018). Plasma-assisted CO₂ conversion: optimizing performance via microwave power modulation. *J. Phys. D: Appl. Phys.*, 51(14).
- [Butylkin et al., 1979] Butylkin, Y. P., Grinenko, A. A., and Ermin, Y. S. (1979). *Sov. Phys. High. Energy Chem.*, 13.
- [Carbone and Nijdam, 2014] Carbone, E. and Nijdam, S. (2014). Ultra-fast pulsed microwave plasma breakdown: evidence of various ignition modes. *Plasma Sources Sci. Technol.*, 23(1).
- [Carbone and Nijdam, 2015] Carbone, E. and Nijdam, S. (2015). Thomson scattering on non-equilibrium low density plasmas: principles, practice and challenges. *Plasma Phys. Control. Fusion*, 57.
- [Chase, 1998] Chase, M. W. (1998). NIST-JANAF Thermochemical tables. *J. Phys. Chem. Ref. Data Mon.*, 9:1–2952.
- [Chen et al., 2017] Chen, G., Britun, N., Godfroid, T., Georgieva, V., Snyders, R., and Deplancke-

- Ogletree, M.-P. (2017). An overview of CO₂ conversion in a microwave discharge: the role of plasma-catalysis. *J. Phys. D: Appl. Phys.*, 50:084001.
- [den Harder et al., 2016] den Harder, N., van den Bekerom, D. C. M., Al, R. S., Graswinckel, M. F., Palomares, J. M., Peeters, F. J. J., Ponduri, S., Minea, T., Bongers, W. A., van de Sanden, M. C. M., and van Rooij, G. J. (2016). Homogeneous CO₂ conversion by microwave plasma: Wave propagation and diagnostics. *Plasma Process. Polym.*, 14.
- [Duten et al., 2002] Duten, X., Rousseau, A., Gicquel, A., Hassouni, K., and Leprince, P. (2002). Time-resolved measurements of the gas temperature in a H₂/CH₄ medium pressure microwave 915 MHz pulsed plasma. *J. Phys. D: Appl. Phys.*, 35.
- [Fridman, 2008] Fridman, A. A. (2008). Plasma Chemistry. *Taylor & Francis Routledge*.
- [Gamache et al., 2014] Gamache, R. R., Lamouroux, J., Blot-Lafon, V., and Lopes, E. (2014). An intercomparison of measured pressure-broadening, pressure shifting parameters of carbon dioxide and their temperatures. *J. Quant. Spectrosc. Radiat. Transfer*, 135:30–43.
- [Goede et al., 2013] Goede, A. P. H., Bongers, W. A., Graswinckel, M. F., van de Sanden, M. C. M., Leins, M., Kopecki, J., Schulz, A., and Walker, M. (2013). Production of solar fuels by CO₂ plasmolysis. *3rd European Energy Conf.*
- [Gordon and McBride, 1994] Gordon, S. and McBride, B. J. (1994). Computer program for calculation of complex chemical equilibrium compositions and applications i. analysis. *National Aeronautics and Space Administration*, (RP-1311).
- [Hartmann et al., 1988] Hartmann, J. M., Rosenmann, L., Perrin, M. Y., and Taine, J. (1988). Accurate calculated tabulations of CO line broadening by H₂O, N₂, O₂, and CO₂ in the 200–3000 K temperature range. *Applied Optics*, 27(15):3063–3065.
- [Hassouni et al., 2001] Hassouni, K., Duten, X., Rousseau, A., and Gicquel, A. (2001). Investigation of chemical kinetics and energy transfer in a pulsed microwave H₂/CH₄ plasma. *Plasma Sources Sci. Technol.*, 10(1).
- [Hbner et al., 2014] Hbner, S., Carbone, E., Palomares, J. M., and van der Mullen, J. (2014). Afterglow of Argon Plasmas with H₂, O₂, N₂, and CO₂ Admixtures Observed by Thomson Scattering. *Plasma Process. Polym.*, 11.
- [Herzberg, 1950] Herzberg, G. (1950). *Molecular spectra and molecular structure Volume II: Infrared and Raman Spectra of Polyatomic Molecules*. Krieger Publishing Company, Malabar, Florida.
- [Jacobs et al., 1974] Jacobs, R. R., Pettipiece, K. J., and Thomas, S. J. (1974). Rotational relaxation rate constants for CO₂. *Appl. Phys. Lett.*, 24(8).
- [Kabouzi and Moisan, 2005] Kabouzi, Y. and Moisan, M. (2005). Pulsed microwave discharges sustained at atmospheric pressure: study of the contraction and filamentation phenomena. *IEEE Trans. Plasma Sci.*, 33.
- [Kochanov et al., 2016] Kochanov, R., Gordon, I., Rothman, L., Wcislo, P., Hilla, C., and Wilzewski, J. (2016). HITRAN Application Programming Interface (HAPI): A comprehensive approach to working with spectroscopic data. *J. Quant. Spectrosc. Radiat. Transfer*, 177:15–30.
- [Koldanov et al., 2005] Koldanov, V. A., Grbachev, A. M., A.L.Vikharev, and Radishev, D. B. (2005). Self-consistent simulation of pulsed and continuous microwave discharges in hydrogen. *Plasma Phys. Rep.*, 31.
- [Legasov et al., 1978] Legasov, V., Vakar, A., Denisenko, V., Maximov, G., Rusanov, V., Fridman, A., and Sholin, G. (1978). *Sov. Phys., Doklady*, 243:323.
- [Li et al., 2015] Li, G., Gordon, I. E., Rothman, L. S., Tan, Y., Hu, S.-M., Kass, S., Campargue, A., and Medvedev, E. S. (2015). Ro-vibrational line lists for nine isotopologues of the CO molecule in the X¹Σ⁺ ground electronic state. *Astrophys. J. Suppl. Series*, 216(1).
- [Lieberman and Ashida, 1996] Lieberman, M. A. and Ashida, S. (1996). Global models of pulse-power-modulated high-density, low-pressure discharges. *Plasma Sources Sci. Technol.*, 5(2).
- [McBride and Gordon, 1996] McBride, B. J. and Gordon, S. (1996). Computer program for calculation of complex chemical equilibrium compositions and applications ii. user’s manual and program description. *National Aeronautics and Space Administration*, (RP-1311-P2).

- [Nishimae and Yoshizawa, 1990] Nishimae, J. and Yoshizawa, K. (1990). Development of CO₂ laser excited by 2.45-GHz microwave discharge. *Proc. SPIE 1225, High-Power Gas Lasers*.
- [Repsilber et al., 2004] Repsilber, T., Baeva, M., and Uhlenbusch, J. (2004). Spatial and temporal characteristics of atomic nitrogen in a pulsed microwave discharge. *Plasma Sources Sci. Technol.*, 13(1).
- [Ring et al., 1995] Ring, Z., Mantei, T. D., Tlali, S., and Jackson, H. E. (1995). Low temperature diamond growth in a pulsed microwave plasma. *J. Vac. Technol. A*, 13.
- [Rothman et al., 2013] Rothman, L. S., Gordon, I. E., Babikov, Y., Barbe, A., Benner, D. C., Bernath, P. F., Birk, M., Bizzocchi, L., Boudon, V., Brown, L. R., Campargue, A., Chance, K., Cohen, E. A., Coudert, L. H., Devi, V. M., Drouin, B. J., Fayt, A., Flaud, J. M., Gamache, R. R., Harrison, J. J., Hartmann, J. M., Hill, C., Hodges, J. T., Jacquemart, D., Jolly, A., Lamouroux, J., Roy, R. J. L., Li, G., Long, D. A., Lyulin, O. M., Mackie, C. J., Massie, S. T., Mikhailenko, S., Mller, H. S. P., Naumenko, O. V., Nikitin, A. V., Orphal, J., Perevalov, V., Perrin, A., Polovtseva, E. R., Richard, C., Smith, M. A. H., Starikova, E., Sung, K., Tashkun, S., Tennyson, J., Toon, G. C., Tyuterev, V. G., and Wagner, G. (2013). The HITRAN 2012 Molecular Spectroscopic Database. *Quant Spectrosc. Radiat Transfer.*, 130:4–50.
- [Rousseau et al., 2004] Rousseau, A., Teboul, E., and Sadeghi, N. (2004). Time-resolved gas temperature measurements by laser absorption in a pulsed microwave hydrogen discharge. *Plasma Sources Science and Technology*, 13(1):166.
- [Rousseau et al., 1994] Rousseau, A., Tomasini, L., Gousset, G., Boisse-Laporte, C., and Leprince, P. (1994). Pulsed microwave discharge: a very efficient H atom source. *J. Phys. D: Appl. Phys.*, 27(11).
- [Rusanov et al., 1981] Rusanov, V. D., Fridman, A. A., and Sholin, G. V. (1981). The physics of a chemically active plasma with nonequilibrium vibrational excitation of molecules. . *Phys Usp.*, 24:447–474.
- [Shahadi et al., 2003] Shahadi, A., Sintov, Y., and Jerby, E. (2003). Longitudinal coupled-cavity scheme for microwave excited CO₂ slab lasers. *Microw. and Optical Tech. Lett.*, 36(2).
- [Silva et al., 2014] Silva, T., Britun, N., Godfroid, T., and Snyders, R. (2014). Optical characterization of a microwave pulsed discharge used for dissociation of CO₂. *Plasma Sources Sci. Technol.*, 23(2).
- [Sintov and Shahadi, 2000] Sintov, Y. and Shahadi, A. (2000). Thermal instability considerations for pulsed microwave excited CO₂ slab lasers. *J. Phys. D: Appl. Phys.*, 33.
- [Snoeckx et al., 2015] Snoeckx, R., Zeng, X. Y., Tu, X., and Bogaerts, A. (2015). Plasma-based dry reforming: improving the conversion and energy efficiency in a dielectric barrier discharge. *RSC Adv.*, 5:274007.
- [Stancu et al., 2005] Stancu, G. D., Pipa, A. V., Lombardi, G., Davies, P. B., Gicquel, A., Lavrov, B. P., and Rpcke, J. (2005). On the Reaction Kinetics of Chemically Active Molecular Microwave Plasmas. *Contr. Plasma Phys.*, 45.
- [Svehla, 1995] Svehla, R. A. (1995). Transport coefficients for the nasa lewis chemical equilibrium program. *National Aeronautics and Space Administration*, (TM-4647).
- [Vakar et al., 1981] Vakar, A. K., Zhivotov, V. K., Karimova, F. F., Krasheninnikov, E. G., Rusanov, V. D., and Fridman, A. A. (1981). Measurement of the vibrational temperature of molecules in a nonequilibrium plasma. *Zh. Tekh. Fiz.*, 7:996–1001.
- [van de Sande and van der Mullen, 2002] van de Sande, M. J. and van der Mullen, J. J. A. M. (2002). Thomson scattering on a low-pressure, inductively-coupled gas discharge lamp. *J. Phys. D: Appl. Phys.*, 35.
- [van den Bekerom et al., 2017] van den Bekerom, D. C. M., den Harder, N., Minea, T., Gatti, N., Linares, J. P., Bongers, W. A., van de Sanden, M. C. M., and van Rooij, G. J. (2017). Non-equilibrium microwave plasma for efficient high-temperature chemistry. *J. Vis. Exp.*, 126.
- [van den Bekerom et al., 2018] van den Bekerom, D. C. M., Nijdam, S., van Veldhuizen, E., van de Sanden, M. C. M., and van Rooij, G. J. (2018). How the alternating degeneracy in rotational Raman spectra of CO₂ and C₂H₂ reveals the vibrational temperature. *Applied Optics*, 57:5694–

5702.

- [van Gessel et al., 2012] van Gessel, A. F. H., Carbone, E. A. D., Bruggeman, P. J., and van der Mullen, J. J. A. M. (2012). Laser scattering on an atmospheric pressure plasma jet: disentangling Rayleigh, Raman and Thomson scattering. *Plasma Sources Sci. Technol.*, 21.
- [van Rooij et al., 2015] van Rooij, G. J., van den Bekerom, D. C. M., den Harder, N., Minea, T., Berden, G., Bongers, W. A., Engeln, R., Graswinckel, M. F., Zoethout, E., and van de Sanden, M. C. M. (2015). Taming microwave plasma to beat thermodynamics in CO₂ dissociation. *Faraday Discuss.*, 183:233–248.